Machined Surface Error Analysis for Laser Micromachining of Biocompatible Polymers for Medical Devices Manufacturing

Deyao Ren[1], Roger J. Narayan[2] and Yuan-Shin Lee[1]

[1]North Carolina State University, dren@ncsu.edu, yslee@ncsu.edu
[2]University of North Carolina at Chapel Hill, roger_narayan@msn.com

ABSTRACT

In this paper, we present the detailed techniques of machined surface errors analysis for laser micromachining of biocompatible polymers. Laser micromachining, with its noncontact characteristics and extensive material selection, is a good fit for micro-scale biomedical devices manufacturing. Machined surface error of laser micromachining is different from that in conventional machining processes and has not been fully addressed yet. In this paper, we present the formulation and modeling techniques to analyze the sources of machined surface errors and to consider the overlapping effects for laser micromachining. An analytical model is proposed to calculate and predict the machined surface errors considering the overlapping effects in laser micromachining. Experimental results based on laboratory experiments are presented for validation of the proposed analytical modeling techniques. The presented techniques can be used in integrating CAD/CAM systems with laser micromachining of biocompatible polymers for medical devices manufacturing.

1. INTRODUCTION

Laser micromachining is based on the removal of material with short and intense laser pulses due to the absorption of laser energy by the material [13]. If the fluence of the laser beam shot onto the material surface is high enough to reach the threshold value (F_{th}) that is required for this material to decompose, the material removal occurs. Controlled by computer and translation stage, laser micromachining system can be used to fabricate desired geometric pattern. UV light is well absorbed by most of materials especially by biological materials and organic compounds [3, 13]. Excimer lasers emit lights in the UV range of 157-355 nm. Compared with high power infrared Nd:YAG and CO_2 lasers, the shorter wavelength of excimer laser is able to achieve better optical resolution [13]. In the excimer laser micromachining, laser energy tends to directly break the molecular bonds inside maerials rather than burn the material due to the very short laser pulse duration, which can help to redue the heat effect around the machining areas.

With the noncontact feature and extensive material selection excimer laser micromachining becomes a competitive candidate in several applications where contamination must be avoided like biomedical device manufacturing in microscale [9]. Many researchers have focused their study on the performance of laser micromachining on various materials including metals [15], semiconductor [1], ceramics [17]

and polymers [2],[4]. Among these categories, polymers show the best machining performance due to their low thermal conductivity and good UV laser energy absorption. Polymer is also an inexpensive alternative and owns the best biocompatible properties. Polymers are good candidates for biomedical applications by laser micromachining. Some techniques were also applied to improve the machined surface quality by laser micromachining such as gas or water medium in the process of machining [16], post processes [4] or short laser pulse duration [7]. These approaches can improve the surface roughness caused by heat or material debris in laser micromachining, but have nothing to do with the machined surface errors caused by adjacent cutting paths.

In laser micromachining, masking is one of the popular approaches to control the laser energy shot on material surface and the geometry of the structures. Through the various sizes of holes on mask, different cutting depth can be achieved. A numerical model was built to represent the relationship between size of holes on mask and cutting depth [5]. Given a depth in 3D, a diameter will be calculated on 2D mask based on numerical model. In [12], a CAD/CAM system for laser micromachining was introduced. The function of CAD/CAM system is very similar to conventional CAD/CAM system including importing standard CAD files, triangulation of object surfaces, slicing the CAD models and generating NC code for tool path and masking layout design. By exploiting the system, the laser influence, pulse repetition frequency and the number of shots per area were studied to optimize the wall angle and ablation depth. Due to uncertain energy losses, variant laser energy profile and irregular cutting shapes, laser machined surface error analysis is not as straightforward as those of the conventional machining processes. A two-stage approach was proposed in [14] to predict cutting performance of laser micromachining by continuous laser pulses, which involved the calculation of the radiation distribution incident on the partially machined surface and modeling of the ablation and removal of materials from the surface. The overlapping effects and stitched errors in laser machining were discussed in [11-12]. Two adjacent cutting paths were considered to calculate the machining error by laser micromachining. However, it is still lack of a general numerical model for the machined surface error analysis in laser micromachining considering the general form of laser energy profile.

In this paper, we present the quantitative techniques of machined surface errors analysis for laser micromachining of biocompatible polymers. A numerical model to calculate and predict the machined surface errors is proposed to include the consideration of variant laser energy profile, irregular cutting shape on materials surfaces, distance between adjacent paths, overlapping effects and continuous laser ablation. We first start the discussion on the shape of laser beam and the energy profile of excimer laser which determines the profile of ablated volume on material surfaces. Then the cutting shape by single laser cutting path will be analyzed. The machined surface errors caused by adjacent cutting paths are analyzed. Practical examples and the results from both experiments and simulation will be compared.
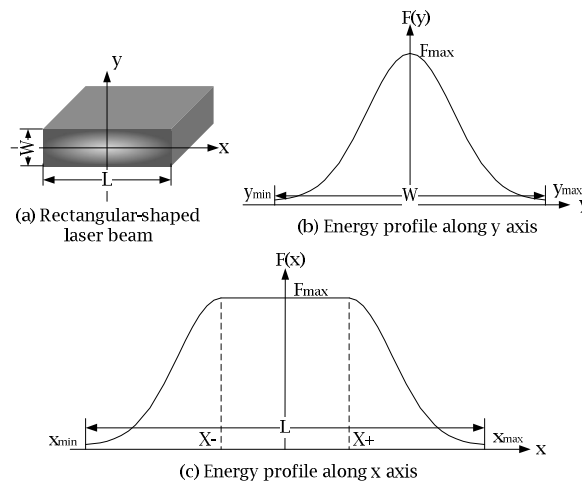
Fig. 1: Rectangular Laser beam with multimodal energy profile of excimer laser.

2. MODELING OF ENERGY PROFILE IN LASER MIROMACHINING

Machined surface errors have been extensively studied for conventional machining processes. In our earlier work, we have studied the key factors of cutter geometry, tool orientation and local geometric features to analyze machined surface errors in CNC machining [10]. In laser micromachining, since materials are removed by energy of laser pulses, there are no real physical cutters in laser micromachining and the traditional techniques of machined surface error analysis cannot be used in laser machining. Thus, it is of interest to study the shape and energy profile of a laser beam for laser micro-machined surface errors analysis.

2.1 Multimode Energy Profile of Laser Micromachining

There are two types of laser beams with different energy profiles: (1) the circular-shaped laser beam with Gaussian energy profile emitted by CO_2, Copper vapor, Ti: Sapphire and Nd: YAG laser, and (2) the rectangular-shaped laser beam with multimode energy profile like TEA CO_2 and excimer laser [13]. An example of rectangular-shape laser beam of excimer laser is shown in Fig. 1(a). The energy distribution along the Y direction of the rectangular-shaped laser beam is shown in Fig. 1(b) and can be approximately formulated as a Gaussian function shown as follows:

$$F(y) = F_{max} e^{-\frac{y^2}{2\sigma^2}} \tag{2.1}$$

where $F(y)$ is the fluence on one point of the laser profile curve; F_{max} is the maximal fluence in this laser beam which is the center of cross section plane; y is the depth direction on the cross section of a laser beam as shown in Fig. 1(a); and σ is a range of laser beam spread over and in this paper σ is selected as

$\sigma = \frac{y_{max} - y_{min}}{6} = W/6$, where W is the dimension of laser beam.

As shown in Fig. 1(c), the laser energy profile along the perpendicular direction X can be formulated as a modified Gaussian functions with a flat modifier function shown as follows:

$$F(x) = \begin{cases} F_{max} & x^- \leq x \leq x^+ \\ F_{max} e^{-\frac{(x-x^-)^2}{2\sigma^2}} & x_{min} \leq x \leq x^- \\ F_{max} e^{-\frac{(x-x^+)^2}{2\sigma^2}} & x^+ \leq x \leq x_{max} \end{cases} \tag{2.2}$$

where $\sigma = \frac{x_{max} - x^+}{3} = \frac{x_{min} - x^-}{3}$. At each cross section along the laser's propagation direction, the laser energy distribution has the same profile as the function $F(x)$ presented in Eq.(2.2). Since even in this direction of rectangular-shaped laser beam the energy distributions on both ends are still Gaussian functions, we will consider the Gaussian energy profile in following sections.

2.2 Modeling of Laser Energy Profile along the Penetration Direction

In laser micromachining, laser beam is focused on the focal plane as a small spot by the objective lens to achieve high laser energy density, as shown in Fig. 2(a). Fig. 2(b) show the laser is focused on the focal plane during laser micromachining. Fig. 2(c) shows that, outside the focal plane, the laser energy profile changes along the laser penetration direction according to Eq. (2.1) and (2.2). At the different locations along the penetration direction, the laser energy profiles are slightly different although they are still following the Gaussian distribution function. It is assumed the laser energy is consumed primarily at the laser ablation on the polymer materials. As shown in Fig. 2(c), the laser energy profile

at a different laser penetration depth is formulated as $F(x)' = F_{max}' e^{-\frac{x^2}{2\sigma'^2}}$ by using Eq. (2.2). Based on the energy conservation, the laser beam energy at different penetration levels has the following relationship (see Fig. 2):

(b) Energy profile on focal plane

(c) Energy profile on The cross section beyond focal plane

(a) Laser beam propagation through objective lens and focal plane
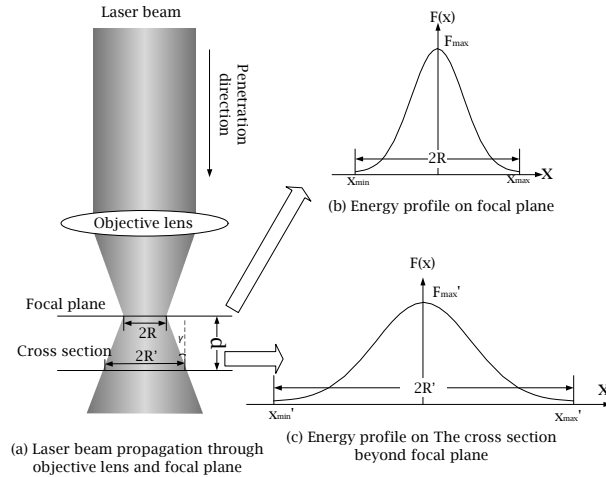
Fig. 2: Change of Laser energy profiles at different penetration depths.

$$\int_{-\infty}^{\infty} F_{\max} e^{-\frac{x^2}{2\sigma^2}} = \int_{-\infty}^{\infty} F_{\max}' e^{-\frac{x^2}{2\sigma'^2}} \tag{2.3}$$

where R and R' representing the laser beam dimension on the focal plane and the cross section plane respectively as shown in Fig 2(b) and (c). We have $\sigma = R/3$ and $\sigma' = R'/3$. Assuming that γ is the angle of the cone shape of laser beam along laser penetration path (see Fig. 2(a)) and d is the distance between the focal plane and cross section plane (see Fig. 2), we have $R' = R + d\tan\alpha$ and $\sigma' = (R + d\tan\gamma)/3$. From Eq.(2.3) we have the following:

$$\int_{-\infty}^{\infty} F_{\max} e^{-\frac{9x^2}{2R^2}} = \int_{-\infty}^{\infty} F_{\max}' e^{-\frac{9x^2}{2(R+d\tan\gamma)^2}} \tag{2.4}$$

By rearranging Eq.(2.4), we can find $F_{\max}'$ at different penetration depth d shown as follows:

$$F_{\max}' = \frac{R}{R + d\tan\gamma} F_{\max} \tag{2.5}$$

Based on Eq. (2.5), the laser energy profile on any cross sections along the penetration depth d can be formulated as the following in terms of the parameters on the focal plane (see Fig. 2(c)):

$$F(x)' = \frac{R}{R + d\tan\gamma} F_{\max} e^{-\frac{9x^2}{2(R+d\tan\gamma)^2}} \tag{2.6}$$

The resultant Eq. (2.6) can be used to determine the laser energy profile $F(x)$ at different laser penetration depth d on the material during laser machining.

When applying the laser beam to machine the materials, only the area that has laser energy larger than the energy threshold will actually cause the ablation of the material. As shown in Fig. 3(a), laser ablation occurs only when the laser fluence $F(x)$ reaches the threshold value F_{th} of the part material. Although the laser beam may cover the area of $[x_{min}, x_{max}]$, the actual ablation area is within the range of $[-x_{th}, x_{th}]$ that have the laser fluence $F(x) > F_{th}$. To perform ablation at the focal plane where $x=x_{th}$, the laser fluence $F(x)$ needs to reach the energy threshold value $F(x) > F_{th}$. As shown in Fig. 3(c), x_{th} is equal to the dimension r of the cavity on focal plane ablated by laser pulse. On the focal plane, the threshold value F_{th} can be formulated as follows:

$$F_{th} = F_{\max} e^{-\frac{9r^2}{2R^2}} \tag{2.7}$$

Figure 3(b) shows the shape of machined cavity and the ablation depth $d(x)$ on the material after the laser ablation. On any of the cross section plane with ablation depth $d > 0$ beyond the focal plane (Fig. 3(b)), ablation occurs when the laser fluence $F(x)$ reaches F_{th}, and the following formulation can be found by using Eq. (2.6) and (2.7):

$$F_{max} e^{-\frac{9r^2}{2R^2}} = \frac{R}{R + d\tan\gamma} F_{max} e^{-\frac{9x_{th}'^2}{2(R+d\tan\gamma)^2}} \tag{2.8}$$

From Eq. (2.8), the ablation width x_{th} on the cross section plane can be found as follows (also see Fig. 3(b)):

$$x_{th}' = r' = \frac{R + d\tan\gamma}{3} \sqrt{2\ln\frac{R}{R + d\tan\gamma} + \frac{9r^2}{R^2}} \tag{2.9}$$

Figure 3(c) show an illustrative example of a laser beam over the area of $[x_{min}, x_{max}]$ and the smaller ablation region of $[-x_{th}, x_{th}]$ given a material ablation energy threshold F_{th}. The above formulation of the laser ablation width and the laser energy profiles will be used to analyze the laser micro-machined surface errors, as detailed in the next sections.

(a) Gaussian laser energy profile

(b) Shape of laser-ablated cavity by single laser path

(c) Laser beam and cavity ablated on machined surface.
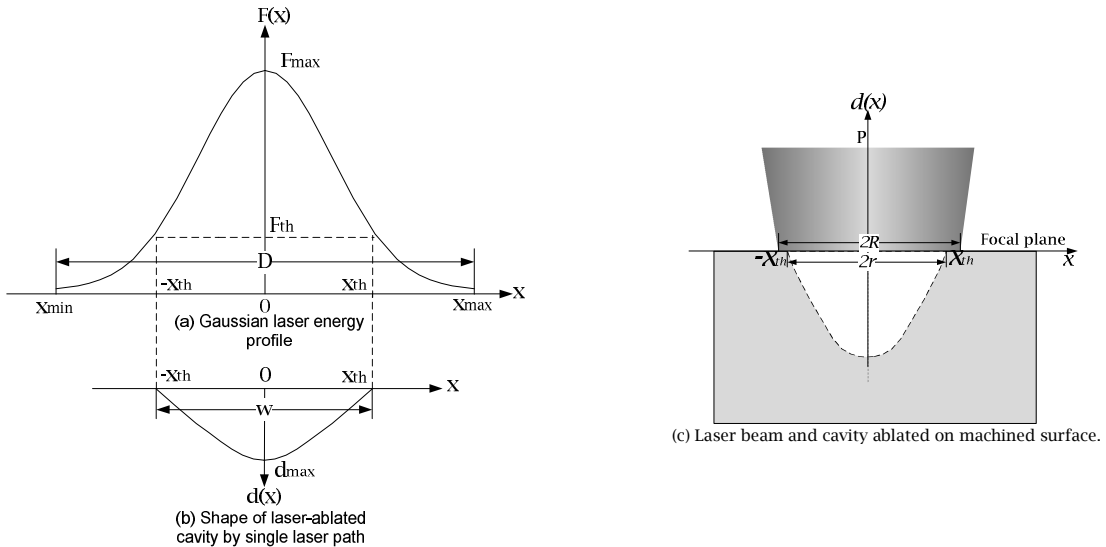
Fig. 3: Energy threshold and laser ablation in machining.

3. MODELLING OF LASER ABLATION ALONG SINGLE LASER TRAJECTORY

To find the machined surface errors caused by adjacent multiple laser paths, we first need to understand the ablation behavior of a single laser trajectory. The primarily governing rule of laser energy absorption is the Beer-Lambert law [13]. Beer-Lambert law is an empirical relationship describing absorption of laser energy to the material through which the laser is travelling. Beer-Lambert law assumes a 1-photon absorption process which is valid for most materials over a limited range of fluence [13]. According to Beer-Lambert law, laser beam intensity $F(x)$ drops exponentially along the laser penetration depth into materials shown as follow:

$$F(d) = F_0 e^{-\alpha d} \tag{3.1}$$

where F_0 (J/cm^2) is the initial beam intensity; α (cm^{-1}) is the absorption coefficient of a particular material; d (cm) is the traveling depth below the material surface. Based on Beer-Lambert law, we can calculate the ablated depth given a material and laser fluence F. Since the laser beam will keep ablating materials until the laser fluence drops under F_{th}, the final ablated depth d by a laser beam with fluence of F_0 measured on material surface can be found by using Eq. (3.1) shown as follows:

$$d = \frac{1}{\alpha} \ln\frac{F}{F_{th}} \tag{3.2}$$

Based on the Gaussian laser energy profile as described in Eq. (2.1), we can calculate the profile of the ablation depth etched by laser pulses based on Eq. (2.1) and (3.2) shown as follows:

$$d(x) = \frac{1}{\alpha}\left(\ln\frac{F_{max}}{F_{th}} - \frac{x^2}{2\sigma^2}\right) \quad (3.3)$$

Using Eq. (3.3), the laser ablation cavity shape described by $d(x)$ can be found (see Fig. 3(b)), based on the given laser energy and the material energy absorption parameters. As shown in Fig. 3(b), the laser ablation energy threshold F_{th} can be found on the material surface when $x \in [-x_{th}, x_{th}]$ and $F = F_{th}$, shown as follows:

$$F_{th} = F_{max} e^{-\frac{x_{th}^2}{2\sigma^2}} \quad (3.4)$$

From Eq. (3.4), the range of the laser ablation $[-x_{th}, x_{th}]$ can be found as follows (see Fig. 3(b)):

$$x_{th} = \sigma\sqrt{2\ln\frac{F_{max}}{F_{th}}} \quad (3.5)$$

The cutting shape by single laser pulse per area can be found using the above mentioned formulation. However, in reality due to the limited machining capacity of a single laser path, multiple numbers of laser pulses in one area are necessary, as shown in Fig. 4. Fig. 4(a) shows that, as the multiple laser pulses being shot on the material, the machined cavity propagates into deeper cavity. Along with the propagation of the machined surface, the laser energy profile $F(x)$ also changes on the intermediate machined surfaces with the instantaneous ablation depth $d(x)$ described earlier in Eq. (2.6), also shown in Fig. 4(b). Therefore, the laser cutting behavior is a combination of multiple laser pulses on partial machined surface in the same area as shown in Fig. 4(a) and (b).

(a) Effects of laser ablation by multiple continuous laser pulses.

(b) Calculation of local laser energy and local cutting depth on partial machined surface.
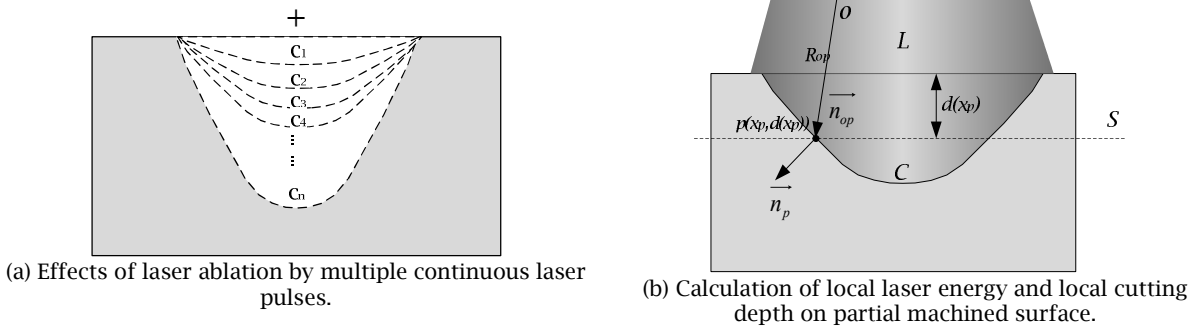
Fig. 4: Effects of multiple pulses in laser ablation and the change of energy profiles.

In Fig. 4(a), C_i is the surface ablated by the first laser pulse L_i and $C_2, C_3, C_4......C_{n-1}$ are the partially machined surfaces ablated by the $2^{nd}, 3^{rd}, 4^{th},......(n-1)^{th}$ laser pulse (L_i) onto the intermediate machined surfaces. In Fig. 4(a), the C_n is final cavity ablated by a total of n laser pulses. To understand the behavior of multiple laser pulses, we need to know the change of the local energy fluence of each laser pulse L_i on the intermediate machined surfaces C_i during the multiple pulses laser machining. As shown in Fig. 4(b), C is the intermediate machined surface. A laser pulse L shoots on C. As shown in Fig. 4(b), $p(x_p, d(x_p))$ is a point on the partially machined surface C and S is a horizontal plane containing point p. Using Eq. (2.6), the energy profile on the surface S can be found as:

$$F(x) = \frac{R}{R + d(x_p)\tan\gamma}F_{max}e^{-\frac{9x^2}{2(R+d(x_p)\tan\gamma)^2}} \quad (3.6)$$

The local laser fluence $F(x)$ at surface point $p(x_p, d(x_p))$ can be formulated as follows (see Fig. 4(b)):

$$F(x_p) = \frac{R}{R + d(x_p)\tan\gamma} F_{max} e^{-\frac{9x_p^2}{2(R+d(x_P)\tan\gamma)^2}} \tag{3.7}$$

Using Eq. (3.7), the laser ablation depth $d(x_p)$ at the local cutting surface C can be found as follows:

$$d(x_p)' = \frac{1}{\alpha}(\ln\frac{\frac{R}{R+d(x_p)\tan\gamma}F_{max}}{F_{th}} - \frac{9x_p^2}{2(R+d(x_p)\tan\gamma)^2}) \tag{3.8}$$

Using Eq. (3.3) and (3.8), for the cavity as shown in Fig. 4(a), the ablation depth along the partially laser machined surface C_1 can be described as follows:

$$d(x)^1 = \frac{1}{\alpha}(\ln\frac{F_{max}}{F_{th}} - \frac{x^2}{2\sigma^2}) \tag{3.9}$$

Using Eq. (3.9), one can find the second partially machined surface C_2 shown as follows:

$$d(x)^2 = d(x)^1 + \frac{1}{\alpha}(\ln\frac{\frac{R}{R+d(x)^1\tan\gamma}F_{max}}{F_{th}} - \frac{9x^2}{2(R+d(x)^1\tan\gamma)^2}) \tag{3.10}$$

Continuing in using Eq. (3.9) and (3.10), the ith partially machined surface C_i can be found as follows (see Fig. 4(a)):

$$d(x)^i = d(x)^{i-1} + \frac{1}{\alpha}(\ln\frac{\frac{R}{R+d(x)^{i-1}\tan\gamma}F_{max}}{F_{th}} - \frac{9x^2}{2(R+d(x)^{i-1}\tan\gamma)^2}) \tag{3.11}$$

The final laser ablation shape C_n by a total of n total laser pulses per area can be formulated as follows (also see Fig. 4):

$$d(x)^n = d(x)^{n-1} + \frac{1}{\alpha}(\ln\frac{\frac{R}{R+d(x)^{n-1}\tan\gamma}F_{max}}{F_{th}} - \frac{9x^2}{2(R+d(x)^{n-1}\tan\gamma)^2}) \tag{3.12}$$

The resultant Eq. (3.12) can be used to find the laser machined surface shape machined by multiple laser pulses along a single laser trajectory on the materials.

When multiple laser pulses are shot onto the partially machined surfaces as shown in Fig. 4(a), Eq. (3.9) – (3.12) need to be adjusted to reflect the continuous laser pulses in machining.. According to the study in [14], the energy fluence is the total flux of the incident radiation integrated over the laser pulse. This determines the dependence of the ablation rate on the angle of incidence. As shown in Fig. 4(b), R_{op} is the laser ray incident at point p, $\overrightarrow{n_{op}}$ represents R_{op} from o to p and $\overrightarrow{n_p}$ is the surface normal at p into material. We define k as $k = \overrightarrow{n_{op}} \bullet \overrightarrow{n_p}$. Using Eq. (3.9) – (3.12), the local energy profile at point p on surface S is modified as follows:

$$F(x_p) = \frac{kR}{R + d(x_p)\tan\gamma} F_{max} e^{-\frac{9x_p^2}{2(R+d(x_P)\tan\gamma)^2}} \tag{3.13}$$

And the local cutting depth on point p is modeled as:

$$d(x_p)' = \frac{1}{\alpha}(\ln\frac{\frac{kR}{R+d(x_p)\tan\gamma}F_{max}}{F_{th}} - \frac{9x_p^2}{2(R+d(x_p)\tan\gamma)^2}) \tag{3.14}$$

Thus we can rewrite equation (3.9)-(3.12) with k as Eq. (3.13) and (3.14) to reflect the incident angle on the partially machined surfaces for continuous laser machining. In the next sections, we will look into analyzing the machined surface errors by multiple adjacent laser trajectories during laser machining.

4. MACHINED SURFACE ERROR ANALYSIS WITH MULTIPLE ADJACENT LASER TRAJECTORIES

Machined surface errors are determined by the cusp height left over the part surfaces between two adjacent machining paths. In conventional machining processes, the machined surface errors are calculated based on the geometric shape of the cutter during the material removal processes [10]. In laser micromachining, several new issues need to be addressed first. Firstly the shape of ablated material volume is determined by the shape of laser beam and its energy profile. Another issue is caused by the laser propagation. Fig. 5(a) shows the overlapping effects by two adjacent laser paths. As shown in Fig. 5(b), the overlapping of the adjacent laser paths causes further ablation onto the cavity surface that was already ablated by the previous adjacent laser path. As shown in Fig. 5(c), the cusp height caused by initial geometric error Δh is changed to $\Delta h'$ (and $\Delta h' < \Delta h$) due to the overlapping effects by the adjacent laser path. To find the accurate laser machined surface errors, we need to analyze the overlapping effects between the adjacent laser paths.
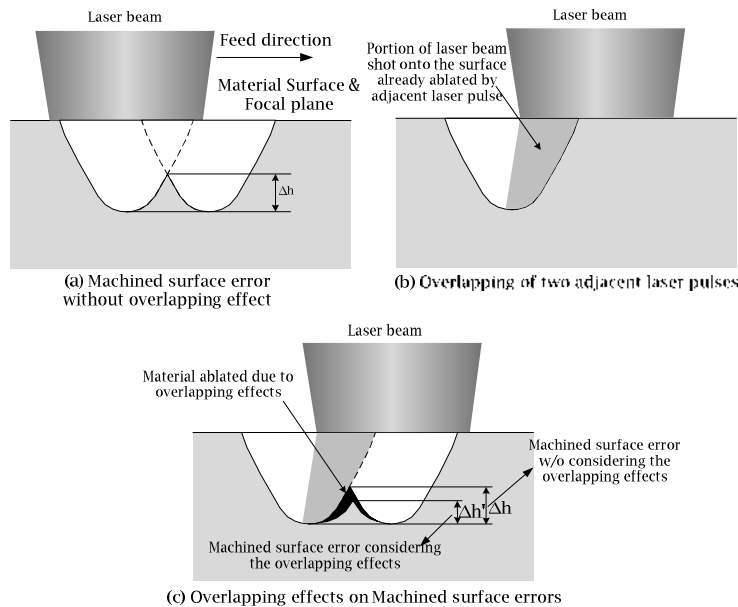
Fig. 5: Machined surface errors caused by overlapping effects between adjacent laser paths.

Fig. 6 shows the part surface machined by multiple adjacent laser paths. As shown in Fig. 6, C_1 is the cavity already ablated by the previous laser path P_1 and C_2 is the cavity that is being ablated by the adjacent laser pulse P_2. As shown in Fig. 6, R is the dimension of laser beam on machining plane, r is the dimension of the opening of cavity ablated by the previous laser path, and δ is the distance between the adjacent laser paths C_1 and C_2. A local coordinate system is defined along the center line of C_2 as the y-axis and the x-axis lying on the machining plane, as shown in Fig. 6. Based on Eq. (2.1),

the energy profile on the machining plane for P_1 can be represented as $F_1(x) = F_{\max} e^{-\frac{9(x+\delta)^2}{2R^2}}$, and the cutting depth function for C_1 can be formulated by using Eq. (3.3) shown as follows:

$$d_1(x) = \frac{1}{\alpha}(\ln \frac{F_{\max}}{F_{th}} - \frac{9(x+\delta)^2}{2R^2}) \qquad x \in [-\delta - r, -\delta + r] \tag{4.1}$$

In Fig. 6, the cusp height $\Delta h(x)$ can be found using the geometric shape of C_1 and C_2 shown as follows:

$$\Delta h(x) = \frac{9(x+\delta)^2}{2\alpha R^2} \qquad x \in [-\delta - r, -\delta + r] \tag{4.2}$$

$M(x_m, d_1(x_m))$ is a point on the surface of C_1 where $x_m \in [\delta + r, \delta - r]$. The distance between the cross section plane of laser beam, which contains point M, and the focal plane can be found as follows (see Fig. 6):

$$d_1(x_m) = \frac{1}{\alpha}(\ln\frac{F_{\max}}{F_{th}} - \frac{9(x_m+\delta)^2}{2R^2}) \tag{4.3}$$

The cusp height $\Delta h(x)$ from point M to bottom of C_1 is found to be

$$\Delta h(x) = \frac{9(x_m+\delta)^2}{2\alpha R^2} \tag{4.4}$$
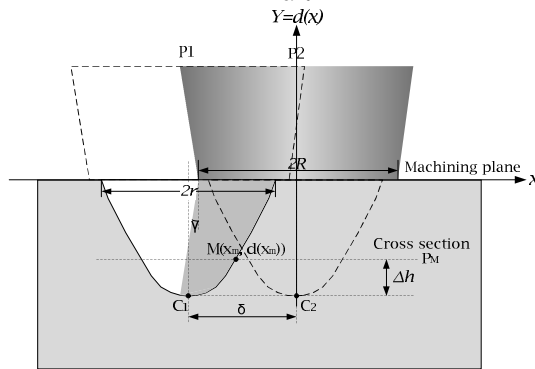
Fig. 6: Calculation of machined surface errors caused by adjacent laser paths.

Now we consider the adjacent laser path P_2 and its overlapping effects on cavity C_1. The laser energy profile of P_2 on the focal plane is $F_2(x) = F_{\max}e^{-\frac{9x^2}{2R^2}}$, and, the laser energy profile on the cross section plane containing point M, can be formulated by using Eq. (2.6) shown as follows:

$$F_{2m}(x) = \frac{R}{R + d_1(x_m)\tan\gamma}F_{\max}e^{-\frac{9x^2}{2(R+d_1(x_m)\tan\gamma)^2}} \tag{4.5}$$

On this cross section plane when $x_m \in \left[-x_{th}', x_{th}'\right]$, the laser fluence $F(x)$ is over the threshold value F_{th} to allow laser ablation happen. From equation (2.9), we can find the correspondent machined cavity width x_{th} as:

$$x_{th}' = \frac{R + d_1(x_m)\tan\gamma}{3}\sqrt{2\ln\frac{R}{R + d_1(x_m)\tan\gamma} + \frac{9r^2}{R^2}} \tag{4.6}$$

Given the existing previous laser path P_1, the ablation occurs again at point M by the second laser pulse P_2, as shown in Fig. 6. From Eq. (3.8), the new ablation depth etched by P_2 at point M can be found as follows:

$$d_2(x_m) = \frac{1}{\alpha}\left\{\ln\frac{\frac{R}{R+d_1(x_m)\tan\gamma}F_{\max}}{F_{th}} - \frac{9x_m^2}{2\left[R+d_1(x_m)\tan\gamma\right]^2}\right\} \tag{4.7}$$

Thus, for any point with $x \in \left[\delta + r, \delta - r\right]$ on the surface of cavity C_1, considering the overlapping effects of adjacent laser pulses, the cusp height $\Delta h(x)$ of the laser machined shapes C_1 can be found by using Eq. (4.4), when there is no further ablation, and Eq. (4.7), when there is continuous ablation by the adjacent laser path, shown as follows:

$$\Delta h(x) = \begin{cases} \frac{9(x-\delta)^2}{2\alpha R^2} - \frac{1}{\alpha}\left\{\ln\frac{F_{\max}}{F_{th}} + \ln\frac{R}{R + d_1(x)\tan\gamma} - \frac{9x^2}{2[R+d_1(x)\tan\gamma]^2}\right\} & condition\ I \\ \\ \frac{9(x-\delta)^2}{2\alpha R^2} & otherwise \end{cases} \tag{4.8}$$

In Eq. (4.8), the first equation indicates the part surface is continuously ablated by the adjacent laser paths (Condition I), and the second equation is for the cusp height when the adjacent laser beam does

not exceed the ablation energy threshold level. Eq. (4.8) can be used to determine the cusp height $\Delta h(x)$ of machined surfaces after laser machining on the part surfaces.

5. LABORATORY EXPERIMENTS AND RESULTS

The proposed techniques of machined surface analysis have been implemented and experiments of practical examples were conducted at our lab at North Carolina State University. To validate the presented analytical model, we have conducted several experiments with a lab-built laser micromachining system as shown in Fig. 7. In this excimer laser micromachining, a commercial laser scriber (COMPexPro 201, Coherent, Inc.) is used as part of the system. This ArF laser emits laser pulses with wavelength at 193 nm and maximum average power of 4 W. The energy of output laser beam can be adjusted up to 400 mJ and the maximum repetition rate is 10/sec. A lab-built laser delivery system including a set of lens, three high UV reflection mirrors, and objective lens carries the laser beam from the laser scriber to material surface. A CCD camera is installed above the objective lens to monitor the machining process. A 3-aixs translation stage (A3200, Aerotech Inc) is used to provide 3-axis synchronized translation motion for machining parts. High UV reflection mirrors are used to change the direction laser beam. An aperture is used to further reduce the laser beam size. However, it also reduces the laser radiance by block part of laser beam. Objective lens focuses laser beam onto material surface to achieve possible highest fluence. The demagnification of objective lens and the size of incoming laser beam determine the laser spot size onto material surface. A laser energy meter is used to calibrate the laser energy on the machining surface. All experiments are conducted on the materials of polyethylene. Polyethylene is a thermoplastic consisting of long chains of the monomer ethylene. Due to its relative good mechanic properties and excellent biocompatibility, polyethylene has extensive applications in many biomedical areas including implants, bulky space filler and so on.
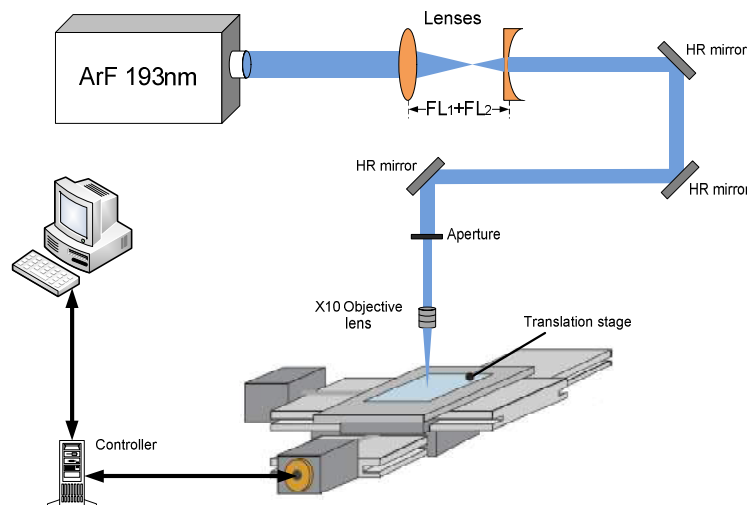
Fig. 7: Lab setup of the excimer laser micromachining system.

In our experiment, micro-channels are fabricated on the material surfaces in our laser micromachining system. The cross sections of these micro-channels are imaged via SEM (Hitachi S-3200N) for measurement purpose. The first experiment is to validate our model for the cutting shape by a single laser path. Number of laser pulses per area is set to 10, 20 and 40. The second experiment is to validate our model to calculate the machined surface errors. In this experiment, two channels are fabricated side by side. The distance between two channels ranges from 25, 30, 35 to 40 μm.

In the first experiment, for each micro-channel fabricated in our laser micromachining system, 20 points are uniformly sampled on its surface (see Fig. 8 and 9). Cutting depth on these 20 points was measured on SEM images and calculated by our simulation program at the same location respectively. The results from both experiments and simulation are listed in Tab. 1 for *number of pulses per area (p)*

=10 and 40, respectively along with the difference between experiment and simulation results. In those tables, *d* means the simulation results while *d'* represents the experiment measurement on one point of the machined surface. The SEM images of the cross section of micro channels and the graphs generated via our simulation program are shown in Fig. 8 and 9 as well. 20 sample points and their cutting depth are plotted on the diagrams in Fig. 8(c) and 9(c). Lines represent the plot of simulation results while dotted lines represent the plot of experiment measurements.

(a) SEM image   (b) Simulation result

(c)Plot of both experiment and simulation results
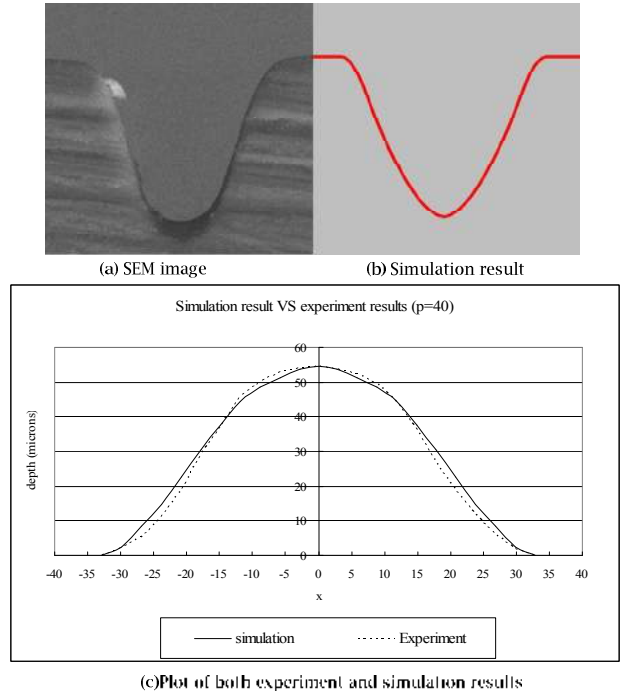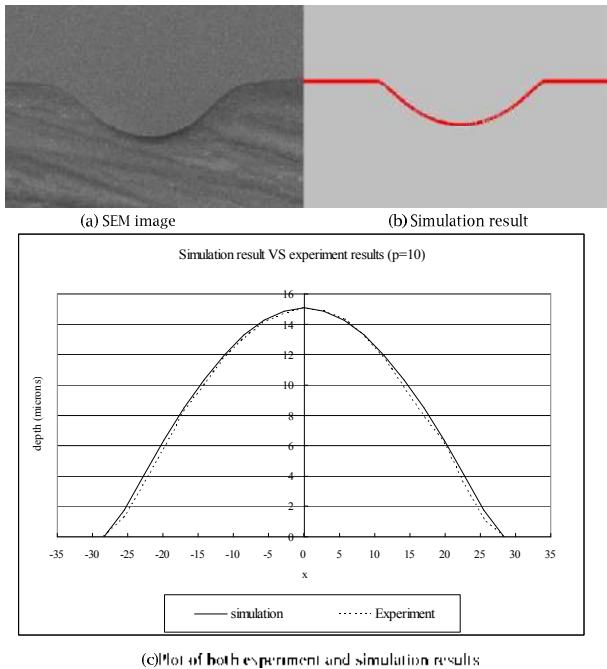
Fig. 8: Comparison of experiment and simulation results (p=10): (a) SEM experiment image; (b) simulation result; (c) plot of experiment measurement and simulation results.

(a) SEM image   (b) Simulation result

(c)Plot of both experiment and simulation results

Fig. 9: Comparison of experiment and simulation results (p=40): (a) SEM experiment image; (b) simulation result; (c) plot of experiment measurement and simulation result.

$x(\mu m)$	-28.39	-25.55	-22.70	-19.87	-17.03	-14.19	-11.35	-8.51	-5.67	-2.83
d(μm)	0.00	1.76	4.09	6.38	8.48	10.34	11.95	13.26	14.25	14.87
d'(μm)	0.00	1.27	3.53	5.72	8.25	9.98	11.79	13.06	14.15	14.69
Error(μm)	0	0.49	0.56	0.66	0.23	0.365	0.16	0.2	0.1	0.18
Percentage	0.00%	38.58%	15.86%	11.54%	2.79%	3.66%	1.36%	1.53%	0.71%	1.23%
$x(\mu m)$	2.83	5.68	8.51	11.35	14.19	17.03	19.87	22.70	25.55	28.39
d(μm)	14.87	14.25	13.26	11.95	10.34	8.48	6.38	4.09	1.76	0.00
d'(μm)	14.87	14.33	13.24	11.79	9.83	7.89	6.17	3.47	1.09	0.00
Error(μm)	0	0.08	0.02	0.16	0.51	0.59	0.21	0.62	0.67	0
Percentage	0.00%	0.56%	0.15%	1.36%	5.19%	7.48%	3.40%	17.87%	61.47%	0.00%

Tab. 1: Experiment measurement and simulation results of cutting shape by single laser path (*p* = 10).

From the results and comparison in Fig. 8 and 9, we can clearly see analytical results and the experiments match with each other very well. It shows our model can accurately predict cutting performance by single path. The second experiment is to validate our model to calculate the machined surface errors. The distances between two adjacent laser pulse range from 25, 30, 35 to 40 μm. The machined surface errors in each case from experiment and simulation are listed as *max(⊿h)* in Tab. 2

along with the *x* value where the machined surface errors occur. The SEM images and the graphs from simulation are shown in Fig. 10.

(a) d=25 μm

(b) d=30 μm

(c) d=35 μm

(d) d=40 μm
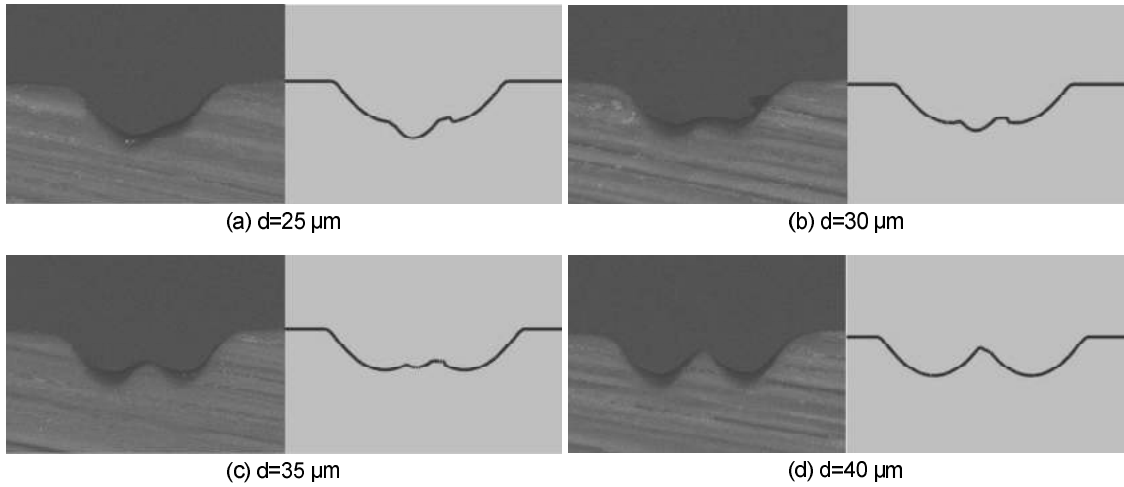
Fig. 10: Machined surface errors measured in experiments (SEM) and analytical result by calculation.

Distance (μm)		25	30	35	40
Simulation	x	9.5	10.5	21.5	21
	max(Δh)	-7.68	-3.7	4.15	9.23
Experiment	x	9.03	10.31	20.64	21.22
	max(Δh)	-7.32	-2.41	3.93	8.89

Tab. 2: Comparison of machined surface errors between experiments and simulations.

The experiment and simulation results are very close to each other, which shows the presented numerical modeling technique can calculate and predict a reasonably accurate machined surface errors given limited input parameter including cutting width, depth and number laser pulses per area.

6. CONCLUSION
In this paper, we have presented an analytical modeling technique to quantitatively calculate the laser micro-machined surface errors given limited inputs including cutting width, depth and number of laser pulses per area. An analytical model is proposed to calculate and predict the machined surface errors considering the overlapping effects in laser micromachining. Experimental results based on laboratory experiments are presented for validation of the proposed analytical modeling techniques. The results from laboratory experiments validate the presented numerical modeling methods by using excimer laser micromachining. The presented techniques can be used to integrate CAD/CAM with the laser micromachining machines to fabricate the desired geometric pattern with satisfied surface roughness for biomedical devices manufacturing.

7. ACKNOWLEDGEMENT

8. REFERENCES
[1] Barsch, N.; Korber, K.; Ostendorf, A.; Tonshoff, K. H.: Ablation and cutting of planar silicon devices using femtosecond laser pulses, Journal of Applied Physics. A 77, 2003, 237-242.
[2] Baudach, S.; Bonse, J.; Kruger, J.; Kautek, W.: Ultrashort pulse laser ablation of polycarbonate and polymethylmethacrylate, Applied Surface Science 154–155, 2000, 555–560.

[3]   Basting, D.; Pippert, K.; Stamm, U.: History and future prospects of excimer laser technology, 2nd International Symposium on Laser Precision Microfabrication, 2001, 14--22.

[4]   Cheng, J.-Y.; Wei, C.-W.; Hsu, K.-H.; Young, T.-H.: Direct-write laser micromachining and universal surface modification of PMMA for device development, Sensors and actuators. B, 99(1), 2004, 186-196.

[5]   Choi, K. H.; Meijer, J.; Masuzawa, T.; Kimm, D. H.: Excimer laser micromachining for 3D microstructures, Journal of Materials Processing Technology, 149(1-3), 2004, 561-566.

[6]   Gai, H.; Voth, G. A.: A computer simulation method for studying the ablation of polymer surface by ultraviolet laser radiation, Journal of Applied Physcis, 71(3), 1992, 1415-1420.

[7]   Le Harzic, R.; Breitling, D.; Weikert, M.; Sommer, S.; Fohl, C.; Valette, S.; Donnet, C.; Audouard, E.; Dausinqer, F.: Pulse width and energy influence on laser micromachining of metals in a range of 100 fs to 5 ps, Applied Surface. Science. 249, 2005, 322–331.

[8]   Kahiert, H.; Sarbach, B.; Burghardt, B.; Klimt, B.: Excimer laser illumination and imaging optics for controlled microstructure generation, Proceedings of SPIE, 1835, 1993, 110-118.

[9]   Klank, H.; Kutter, J. P.; Gescheke, O.: CO2-laser micromachining and back-end processing for rapid production of PMMA-based microfluidic systems, Lab Chip, (2), 2002, 242-246.

[10]   Lee, Y. S.; Chang, T. C.: Machined surface error analysis for 5-axis machining, International Journal of Production Research, 34(1), 1996, 111-135.

[11]   Mutapcic, E.; Iovenitti, P.; Hayes, J. P.: Overlay error effects on polycarbonate structures produced by 248 nm UV laser ablation tool, Proceedings of the 3rd Asia-Pacific Forum on Precision Surface Finishing and Deburring Technology, 2003, 269–280

[12]   Mutapcic, E.; Iovenitti, P.; Hayes, J. P.: A prototyping and microfabrication CAD/CAM tool for excimer laser micromachining process, The International Journal of Advanced Manufacturing Technology, 30 (11-12), 2006, 1076-7083.

[13]   Naessens, K.: Excimer laser ablation of microstructure in polymers for photonic application, Ph.D. dissertation, Ghent, Dutch, 2003.

[14]   Paterson, C.; Holmes, A. S.; Smith, R. W.: Excimer laser ablation of microstructures: A numerical model, Journal of Applied Physics, 86(11), 1999, 6538-6546.

[15]   Pfleging, W.; Hanemann, T.; Torge, M.; Bernauer, W.: Rapid fabrication and replication of metal, ceramic and plastic mould inserts for application in microsystem technologies, Journal of Mechanical Engineering Science, 217(1), 2003, 53-63.

[16]   Ren, J.; Kelly, M.; Hesselink, L.: Laser ablation of silicon in water with nanosecond and femtosecond pulses, Optics Letters, 30(13), 2005.

[17]   Wang, X.; Shephard, J. D.; Dear, F. C.; Hand, D. P.: Optimized nanosecond pulsed laser micromachining of Y-TZP Ceramics, J. Am. Ceram. Sco., 91(2), 2008, 391-397.